Variations of infiltration and electronic contact in mesoscopic perovskite solar cells revealed by high-resolution multi-mapping techniques

Harry Lakhiani,[a] Tom Dunlop,[a] Francesca De Rossi,[a] Stoichko Dimitrov,[a] Robin Kerremans,[b] Cécile Charbonneau,[a] Trystan Watson,[a] Jérémy Barbé[a,] and Wing Chung Tsoi[a,]**

[a]SPECIFIC, College of Engineering, Swansea University, Bay Campus, Fabian Way, Swansea, SA1 8EN, UK

[b]Department of Physics, Swansea University, Singleton Campus, Sketty, Swansea SA2 8PQ, UK

ABSTRACT A combination of high-resolution mapping techniques were developed to probe the homogeneity and defects of mesoscopic perovskite solar cells. Three types of cells using a one-step infiltration process with methylammonium lead iodide ($MAPbI_3$) or 5-ammoniumvaleric acid-$MAPbI_3$ solutions, or two-step process with $MAPbI_3$ solution were investigated. The correlation between photoluminescence, photocurrent, electroluminescence and Raman maps gives a detailed understanding of the different infiltration mechanisms, electronic contact at interfaces and effect on local photocurrent for the cells. One-step $MAPbI_3$ cell has very limited infiltration of the perovskite solution which results in poor device performance. High loading of the mesopores of the TiO_2 and ZrO_2 scaffold is observed when using 5-ammoniumvaleric acid, but some micrometer-sized non-infiltrated areas remain due to dense carbon flakes hindering perovskite infiltration. The two-step cell has a complex morphology with features having either beneficial or detrimental effects on the local photocurrent. Our results provide key insights to achieve better infiltration and homogeneity of the perovskite film in mesoporous devices but can also serve further work on planar devices to develop efficient extraction layers. Besides, this multi-mapping approach allows the correlation of the local photo-physical properties of full perovskite devices, which would be challenging to obtain by other techniques.

KEYWORDS: mesoscopic perovskite solar cells, photocurrent, photoluminescence, Raman, electroluminescence, mapping, infiltration, electronic contact.

Carbon-based hole-conductor-free mesoscopic perovskite solar cells (C-PSCs) have emerged as one of the most promising perovskite solar cell architectures, in terms of low cost of materials, ease of manufacture and long-term stability,[1],[2] as well as environmental impact/carbon footprint.[3] Consisting of an all-printable triple mesoscopic stack, *i.e.* titania (TiO_2) scaffold, insulating layer (either ZrO_2 or Al_2O_3) and carbon-based back electrode, lab scale C-PSCs have achieved 15.9% PCE for a methylammonium lead iodide ($MAPbI_3$) perovskite chemically modified by adding $SrCl_2$,[4] and 17% PCE when a triple cation

perovskite is used as the absorber.[5] While still lagging behind other types of PSCs, in terms of efficiency (record PCE for mesoporous TiO_2-based PSCs with organic HTM and evaporated metal electrode is over 22%),[6],[7] C-PSCs have demonstrated unprecedent long-term stability: over 1 year under continuous AM1.5 illumination and over 1000 hours under different conditions of illumination and external stresses, even for un-encapsulated cells.[8],[9] Large area modules have been reported by different groups, with PCE over 10% on 10 x 10 cm^2 substrates,[9],[10],[11],[12] and around 6% for A4 sized modules.[13] In addition, the lack of expensive metal cathode[14] and organic HTM,[15] use of abundant materials, easy printing processes and low capital cost equipment also account for simpler and cheaper manufacturing process, paving the way for C-PSCs to move quickly from the lab to the market.

Unlike spin-coating, perovskite precursors solutions are infiltrated into the mesoporous triple stack with little waste of material, via drop casting, ink-jet printing or automatized dispensing.[16] When using DMF or DMF:DMSO as solvents, a good infiltration of the thick stack (usually >10 µm) is achieved for both one-step[17] and two-step deposition.[18] However, for large scale production it is critical to replace DMF with less toxic solvent such as gamma-Butyrolactone (GBL). It was shown that when using GBL solvent, 5-ammonium valeric acid iodide (AVAI) should be added to the $MAPbI_3$-GBL precursors solution to improve the wettability and induce better pore filling.[1] Furthermore, AVAI promotes the formation of a characteristic multi-dimensional 2D/3D perovskite junction, responsible for the remarkable long-term stability of this type of cells.[9] Beside solvents, processing variables, such as temperature and humidity, can affect the infiltration throughout such a thick structure, potentially resulting in local variations in the perovskite crystallisation that might be levelled up and hindered when assessing the device via J-V measurements.

In this work, we developed advanced multi-mapping techniques to spatially investigate the device uniformity and defects in C-PSCs based on different infiltration processes using GBL solvent: one-step process with $MAPbI_3$-GBL or AVAI-$MAPbI_3$-GBL precursors solutions, or two-step process with $MAPbI_3$-GBL precursors solution. Recently, researchers have probed spatial variations in local photoluminescence and photocurrent of planar inverted-type PSCs and suggested variability in contact to the active layer, which causes local carrier extraction heterogeneity and eventually impacts the device performance.[19],[20] However, to our knowledge, no such study has been carried out on mesoscopic PSCs in which the contact properties between the perovskite layer and the extraction layers might be radically different due to the mesoporous structure of the device itself and the infiltration process used in this case. Here, for the first time photoluminescence (PL), electroluminescence (EL), Raman and photocurrent maps are acquired on the same area with high resolution. On the contrary to imaging techniques,[21] these maps are spectrally and spatially resolved which means that the PL, EL and Raman spectra are acquired for each data point. Hence, information such as PL and EL peak width and position, and Raman maps for selected peaks can be extracted from these data, which allows not only to gain information about spatial heterogeneities but also to identify the nature of the observed features. The PL intensity alone can be complex to interpret in a full device structure as competing mechanisms such as charges quenching and non-radiative recombination may happen simultaneously. However, using complementary techniques such as PL, EL and photocurrent mapping allows to gain better understanding of mesopore filling by the perovskite solution and electronic coupling with the extraction layer. These techniques are carried out on full devices in a non-destructive way so that they provide a relatively simple inspection tool which allows to correlate the overall PV performance to the device defects and homogeneity.

RESULTS AND DISCUSSION

Current voltage characteristics

The performance of the mesoscopic perovskite solar cells prepared using different solutions and deposition processes were first characterized under 1 sun AM1.5g illumination and the results are shown in Figure 1. It is important to consider that the

performance of this type of cells depends on the masked area exposed to light during the J-V measurements, due to the poor conductivity of the carbon top electrode which limits the fill factor:[18] the smaller the masked area, the higher the FF and PCE. The 1 cm^2 active area was masked to 0.5 cm^2 to have more realistic measurements of the device operation. A striking difference in performance was observed between the cells infiltrated via one-step deposition with $MAPbI_3$ and AVAI-$MAPbI_3$: the one-step $MAPbI_3$ delivers just 0.3% PCE due to very poor J_{sc} value, whereas the one-step AVAI-$MAPbI_3$ has 9.0% PCE. Although this value is lower than PSCs using the conventional architecture, it is in line with the values reported for C-PSCs.[18] To obtain higher efficiencies without using AVAI, a two-step infiltration method is preferable: a PbI_2 solution in DMF is infiltrated into the mesoscopic stack, which is then immersed in a MAI solution in IPA to promote the conversion to $MAPbI_3$.[18],[16] However, the two-step $MAPbI_3$ cell is not as efficient as the one-step AVAI-$MAPbI_3$ (4.3% vs 9.0% PCE and J_{SC} of 13.1 vs 22.0 $mA.cm^{-2}$, respectively), which is mostly due to smaller fill factor and J_{sc}.

(a)

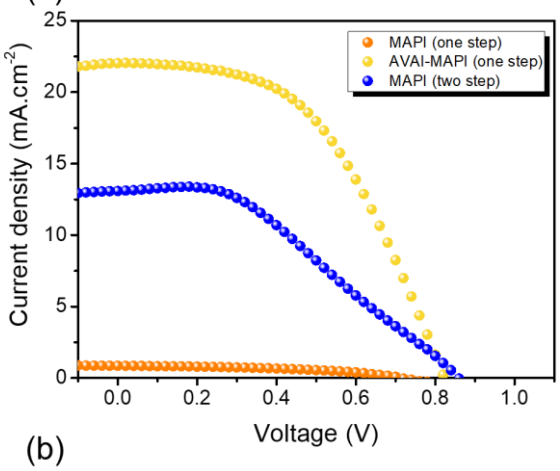

(b)

	Voc (V)	Jsc (mA.cm-2)	FF (%)	PCE (%)
One-step $MAPbI_3$	0.71	0.8	47.2	0.3
One-step AVA-$MAPbI_3$	0.82	22.0	49.8	9.0
Two-step $MAPbI_3$	0.86	13.1	38.3	4.3

Figure. 1 (a) J-V curves under 1 sun AM1.5G illumination of mesoscopic perovskite solar cells fabricated using one-step $MAPbI_3$, one-step AVAI-$MAPbI_3$ and two-step $MAPbI_3$ processes. (b) PV parameters measured for the three types of cells.

High-resolution multi-mapping

In order to understand the significant variations in performance of the different types of cells under solar spectrum, the cells were characterized under nitrogen atmosphere by high-resolution photoluminescence, photocurrent, electroluminescence and Raman mapping on 500 x 500 µm and 20 x 20 µm areas using a Renishaw InVia confocal Raman microscope. All maps and optical images were taken from the substrate side. For PL, photocurrent and Raman maps, a 532 nm laser is transmitted through the glass/FTO/compact TiO_2 layer before being absorbed within the perovskite infiltrated in the mesoporous structure. The calculated excitons generation profile in C-PSCs at 532 nm is shown in Figure S1. Assuming that perovskite has fully infiltrated the mesoporous structure, more than 93% of carriers are generated in the perovskite within the mp-TiO_2 layer. While the PL and photocurrent techniques will give evidences on the variations in charges extraction/electronic coupling between the perovskite and the mp-TiO_2 extraction layer, Raman spectroscopy will provide us with a direct experimental assay of perovskite infiltration. Indeed, if perovskite has not fully infiltrated the mp-TiO_2, enhanced mp-TiO_2 Raman signal will be measured in this case. Hence,

PL/photocurrent and Raman mapping are complementary and allow to discriminate between the effects of lower electronic contact at the interface and poor perovskite infiltration. For EL map, an electrical bias is applied between the carbon and FTO electrodes. The injection of charges at the different interfaces as well as the electrical properties of the different layers in the entire stack can influence the resulting map.

The complete set of maps for the cell prepared using one-step process with $MAPbI_3$ solution (without AVAI) is shown in Figure 2. The 500 x 500 μm optical microscopy image in Figure 2a reveals a clearly non-uniform film with micrometre-sized dark circular features randomly distributed over the device (indicated by orange dashed circles). The PL intensity map spatially correlates well with the optical image and indicates that these features have lower PL intensity as compared to surrounding regions. The photocurrent map acquired simultaneously is in excellent agreement with the optical image and PL maps, and indicates a significant increase in photocurrent where the features are observed. This spatial correlation between low PL intensity and higher photocurrent can be explained by better charge extraction from these regions reducing the yield of radiative recombination in these areas and suggesting the presence of 'hot' spots with better electrical contact between the perovskite and mp-TiO_2.

To study these hot spots further, we extended the capabilities of our mapping technique to detect changes in PL peak position and full width at half maximum (FWHM). In recent works, researchers have focused on PL intensity only[19],[22] but to our knowledge there is no such study showing variations in PL peak position and width in perovskite solar cells. The maps presented in Figure 2a reveal a clear red-shift and narrowing of the photoluminescence at the higher photocurrent 'hot' spots. We hypothesize that the better contact and electronic coupling between the perovskite active material and mp-TiO_2 ETL allows photogenerated electrons in the conduction band to be extracted at short circuit before they can recombine radiatively. This results in reduced band-to-band recombination flux and emission arising from slower charges, likely thermally-activated from shallow defects, as described in Figure S2. On the contrary, in regions of poor electrical contact, PL emission originates from higher energy band-to-band emission because charges extraction rates are slower than emission. This mechanism could also explain the narrower PL FWHM at the 'hot' spots where the charge extraction flux is much higher than the emission, thus reducing the density of emissive charge carriers to those close in energy to the band edge. However, the photoluminescence line width is also an indication of the structural disorder present in the perovskite crystal.[23] Hence, se suggest that the perovskite crystals may have significantly less trap states at the high photocurrent regions, which could be explained by passivation of trap states at the perovskite surface in contact with the mp-TiO_2 ETL. We note that other samples using the same one-step infiltration process have been measured and showed similar optical and electronic properties, as shown in the 100 x 100 um maps in Figure S5. This suggests that the observed non-uniformities are a result of the infiltration process itself and do not vary significantly from batch-to-batch.

From the large map, a region showing a typical 'hot' spot with lower PL intensity/higher photocurrent was selected to perform higher resolution 20x20 μm maps with 1 μm step size shown in Figure 2b. This feature is representative of the other features observed on the large map in Figure 2a, which have similar PL and photocurrent properties. Mapping smaller areas allows to obtain more detailed maps on specific features, but also enables acquiring the EL and Raman maps which are more difficult to perform on a large scale as they require longer acquisition time in order to obtain sufficient signal-to-noise ratio (which might also degrade the device). On the contrary to the PL map which lateral resolution is limited by the size of the laser beam exciting the sample, for the EL map photons are generated by an electrical bias which is applied to the entire cell. In this case, the resolution of the map is dependent on several factors such as the lens numerical aperture, slit size and CCD area. A trade-off between lateral resolution and signal intensity is necessary, which explains why the resolution of the EL map is rather low as compared to the other maps. However, from the EL intensity map, it is quite clear that the 'hot' spot has higher EL intensity than surrounding regions. This reveals better charge injection at these regions, in good agreement with charge quenching indicated by the PL and photocurrent maps.[21] Even if the PL, EL and photocurrent maps clearly demonstrate heterogeneities in local charges extraction/injection, these techniques only are not sufficient to reveal the role played by perovskite infiltration.[19] Hence, a Raman map was performed on

the same region. On the contrary to other mapping techniques used in this work, Raman is a chemical probe which gives direct information about the chemical phases present in the device, independently from electronic processes involved in the device structure. $MAPbI_3$ has a weak Raman signal and would require long acquisition time to get sufficient signal-to-noise ratio, which could be harmful for the cell.[24] Instead, it is more appropriate to display the more intense peak of anatase phase of TiO_2 at 144 cm^{-1} as shown in Figure 2b.[25] Due to the high absorption coefficient of perovskite, $MAPbI_3$ has a "shielding" effect on the TiO_2 signal. The darker region at the centre of the map indicates that less TiO_2 is probed by the laser because perovskite material can absorb the laser before it penetrates deeper in the structure, as a result of better infiltration (single point spectra are shown in Figure 2b next to the Raman map). For comparison, the TiO_2 Raman map of an empty mesoporous stack (before perovskite infiltration) shown in Figure S3b along with a typical Raman spectrum extracted from this map indicates a rather uniform and intense signal from the mp-TiO_2 layer at 144 cm^{-1} as there is no perovskite to block the penetration of the laser beam in the layer stack. Even if the mp-TiO_2 film may have some slight thickness variations as observed in Figure S3b, it cannot explain the signal variations shown in Figure 2b, which is almost one order of magnitude higher outside the dark spot than inside.

This therefore shows that all the different maps acquired on the perovskite solar cell using one-step $MAPbI_3$ infiltration process are consistent with poor infiltration of the layer stack. Only randomly dispersed micrometre-sized areas are well infiltrated with perovskite and provide sufficient electronic contact with the mp-TiO_2 to participate in the photocurrent delivered by the cell, whereas most of the cell is ineffective. This explains why the J_{sc} measured for this cell is less than 1 $mA.m^{-2}$ as most of the incident light is not absorbed in the perovskite within the mp-TiO_2 layer but deeper in the layer stack (in ZrO_2 or carbon). In Figure S4, an optical image of the one-step $MAPbI_3$ device was processed to show a clear contrast between infiltrated and non-infiltrated areas. It was measured that well infiltrated regions represent around 4% of the whole device only. Hence, if the whole device was efficiently infiltrated, the J_{sc} could be multiplied by 25 and reached up to 20 $mA.cm^{-2}$, which is similar to the one-step AVAI-$MAPbI_3$ device.

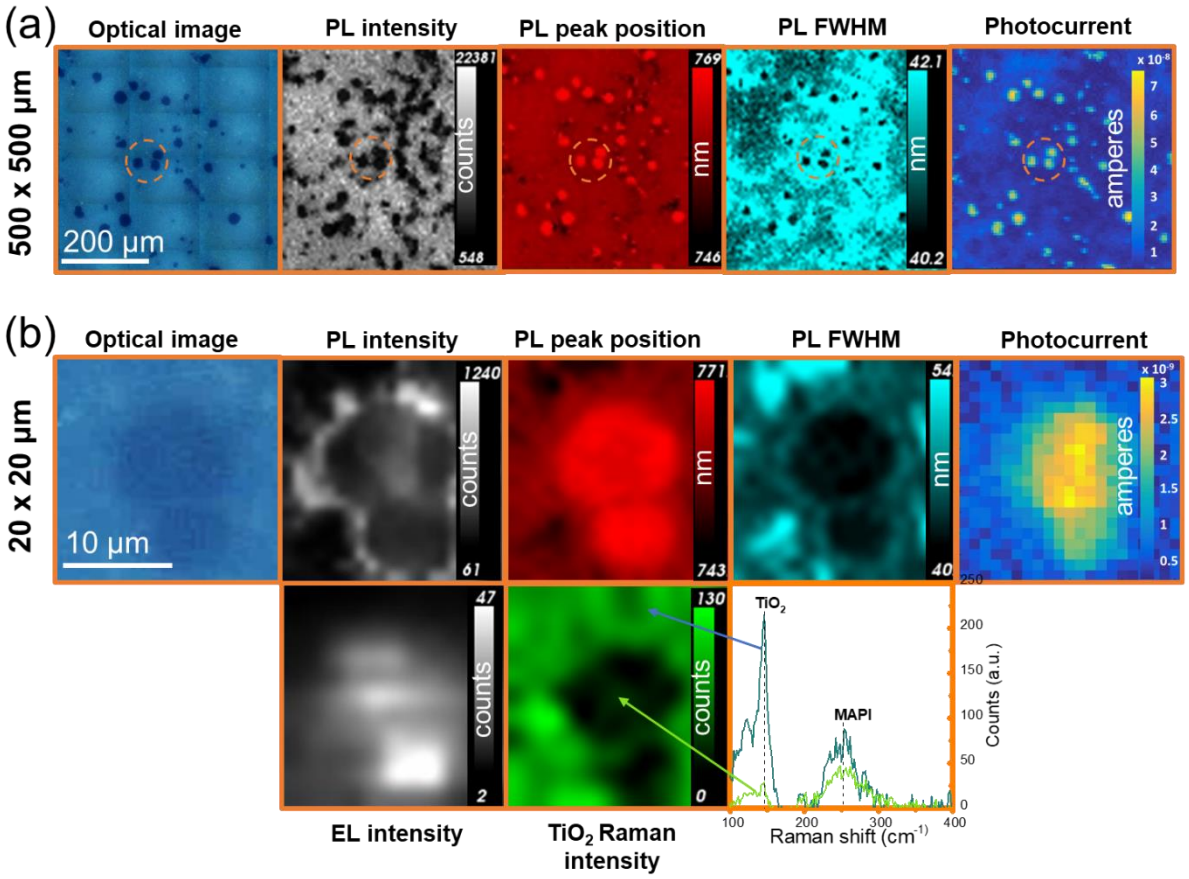

Figure. 2 High-resolution multi-mapping of mesoscopic solar cells fabricated from one-step $MAPbI_3$ solution process. (a) 500 x 500 µm optical microscopic image, PL peak intensity, PL peak position, PL full width at half maximum (FWHM) and photocurrent maps (measured with 1.5 µW laser power). Dashed circles indicate well-infiltrated regions of high photocurrent with narrowed and red-shifted PL. (b) 20 x 20 µm optical image, PL peak intensity, PL peak position, PL FWHM, photocurrent (measured with 0.3 µW laser power), electroluminescence intensity and Raman TiO_2 peak intensity maps measured across a typical feature. Raman single point spectra between 100 cm^{-1} and 400 cm^{-1} measured on and off the feature are also shown.

Then, the same set of maps was acquired on the cell using a one-step infiltration process with AVAI-$MAPbI_3$ solution, as shown in Figure 3. Although exact same mapping parameters were used, critically different results were obtained for this type of device. At first glance, from the 500 x 500 µm optical microscopy image in Figure 3a the one-step AVAI-$MAPbI_3$ device looks much more uniform than the one-step $MAPbI_3$ device described before. Small bright features can be observed, much smaller than the dark features observed in Figure 2a. The PL maps shown in Figure 3a indicate that these features have lower PL peak intensity, lower wavelength and higher width than the surrounding area. The photocurrent map indicates highly uniform photocurrent across the device. However, it can be seen that four spots have significantly higher photocurrent as compared to the rest of the mapped area (□120 nA against □70 nA). The distance of exactly 300 µm between these spots corresponds to the size of the mesh used to print the carbon electrode by screen printing. We believe that the carbon is thinner at the mesh intersections, which could help to infiltrate the perovskite solution, resulting in better charge extraction and reduced recombination. However, most of the device is uniform so that higher resolution maps are needed to have detailed information about the inhomogeneities present in the layer stack. Figure 3b shows 20x20 µm optical image, PL, photocurrent, EL and TiO_2 Raman peak intensity maps taken around a typical bright feature.

It shows clear decrease in PL intensity, which also corresponds to a decrease in photocurrent and decrease in EL intensity. The correlation low PL/low photocurrent/low EL is different from the results obtained with the one-step $MAPbI_3$ sample (low PL/high photocurrent/high EL correlation) and can be explained by poor perovskite infiltration at these regions. Indeed, if the mp-TiO_2 pores are not properly filled with perovskite phase, the reduced amount of perovskite material induces lower PL signal because of scattering effect in the mp-TiO_2 structure, but also lower photocurrent and lower EL due to inefficient electron transport at the perovskite/mp-TiO_2 interface. In good agreement with these results, the TiO_2 Raman map in Figure 3b also indicates higher TiO_2 signal at the centre of the map because of the reduced amount of perovskite in this area. Based on the previous discussion, the PL blue-shift and broadening at the defect location are also in good agreement with electrons in the conduction band not being quenched because of inefficient contact with the mp-TiO_2 extraction layer. Hence, on the contrary to the one-step cell using $MAPbI_3$ solution, the cell using AVAI-$MAPbI_3$ solution is much more uniform and displays excellent perovskite infiltration, which induces efficient charge transport through the device. Although some areas of poor infiltration and reduced photocurrent remain, they represent only 2% of the whole surface (Figure S4). We note that on the contrary to Figure 2a which shows that well-infiltrated regions have circular shape, these areas of poor infiltration have random shape as observed in Figure 3b. The circular shape can be explained by radial diffusion of the perovskite solution once in contact with the c-TiO_2 interface, while the random shape is determined by the shape of the feature blocking perovskite infiltration (*i.e.* dense carbon flake as discussed later).

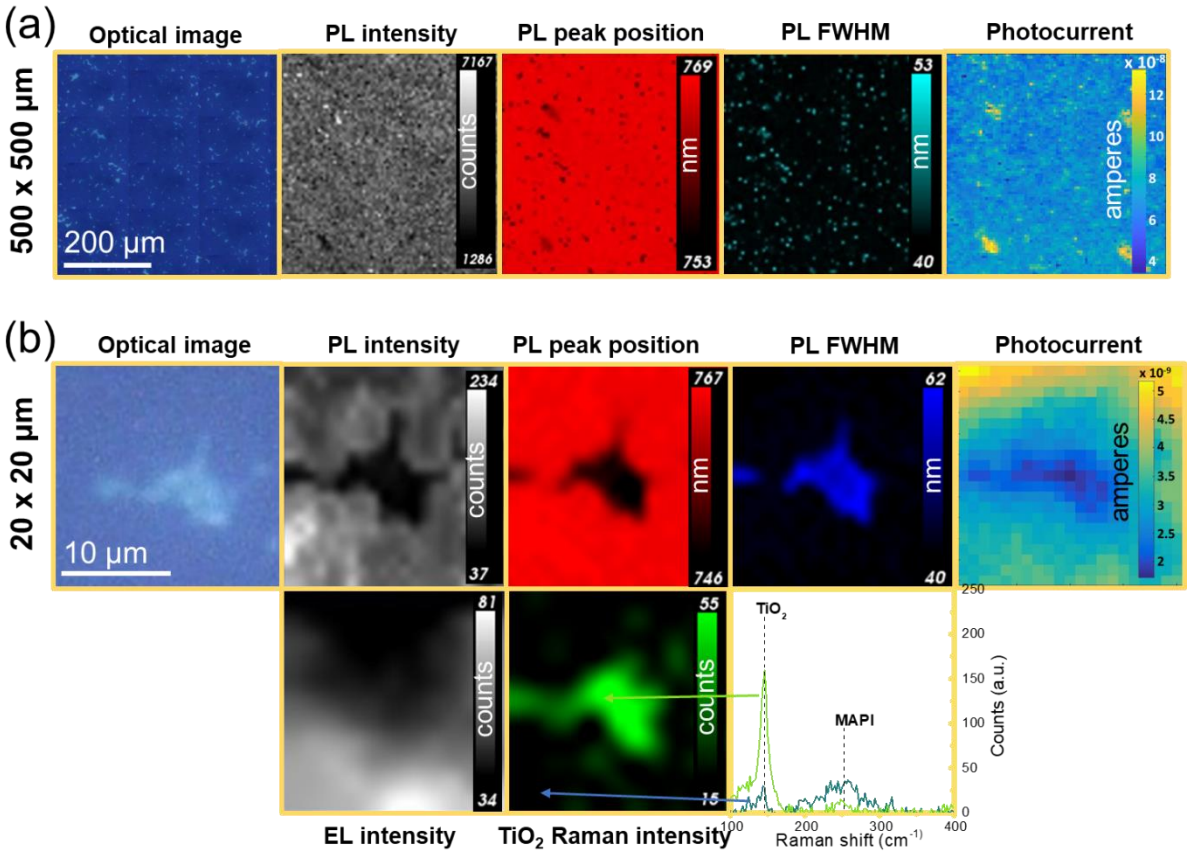

Figure. 3 High-resolution multi-mapping of mesoscopic solar cells fabricated from one-step AVAI-$MAPbI_3$ solution process. (a) 500 x 500 µm optical microscopic image, PL peak intensity, PL peak position, PL FWHM and photocurrent maps (measured with 1.5 µW laser power). (b) 20 x 20 µm optical image, PL peak intensity, PL peak position, PL FWHM, photocurrent (measured with

0.3 μW laser power), electroluminescence intensity and Raman TiO_2 peak intensity maps measured across a typical feature. Raman single point spectra between 100 cm^{-1} and 400 cm^{-1} measured on and off the feature are also shown.

Finally, Figure 4 shows the set of maps acquired on the device using a two-step infiltration process. The 500 x 500 μm optical microscopy image in Figure 4a shows a very different pattern from the two previous samples (vertical and horizontal lines are due to the microscope montage). The centre of the image is rather uniform but large bright areas are observed on the top-right and bottom left of the image. The PL intensity map shows large regions of higher PL intensity and some smaller features with lower PL intensity, which are not clearly seen on the microscopy image. The photocurrent map also reveals large variations in photocurrent, which do not clearly correlate with the PL map or microscopy image (higher resolution maps at three different locations are shown in Figure S8 in SI). In fact, on the contrary to both one-step devices for which the observed features are only related to infiltration mechanisms, the two-step device is more complex and has several types of features/defects across the mapped area with various PL/photocurrent correlations. Indeed, PbI_2 is first infiltrated within the structure which means that variations in PL and photocurrent might come from incomplete mesopores infiltration by the PbI_2 solution and/or non-uniform PbI_2 nucleation. Then, as PbI_2 reacts with MAI, another type of non-uniformity could originate from PbI_2 not being fully converted to $MAPbI_3$ during the dipping process. This is likely to happen considering the relatively thick layer stack (especially as the active perovskite is in the mp-TiO_2, which means that MAI needs to infiltrate deep in the layer stack). In Figure 4b, high-resolution maps were taken around a feature having lower PL intensity, higher photocurrent and higher EL intensity. This feature is not representative of all features observed on the large map because several types of defects are formed for this sample but is interesting as it shows properties not observed for both one-step devices. This correlation can be ascribed to better charge quenching and injection at the interface but as the TiO_2 Raman map is rather uniform for the entire mapped area, it means that the observed feature is not due to infiltration inhomogeneity and should be explained by a different mechanism. In a previous work, we have shown that a very thin PbI_2 film can passivate the interface between the perovskite and extraction layers, which helps to extract charges and results in slightly higher photocurrent.[26] Here, the observed results can be explained similarly: some PbI_2 may not have fully converted to $MAPbI_3$ in the mp-TiO_2 layer close to the c-TiO_2 blocking layer, and could help to extract electrons as long as this residual PbI_2 is thin enough (too thick PbI_2 would induce higher series resistance and lower photocurrent). Hence, for the two-step device it is thought that the large variations observed in the PL and photocurrent maps with diverse correlations could be due to several distinct defects such as poor PbI_2 infiltration, non-uniform nucleation and incomplete conversion of the PbI_2.

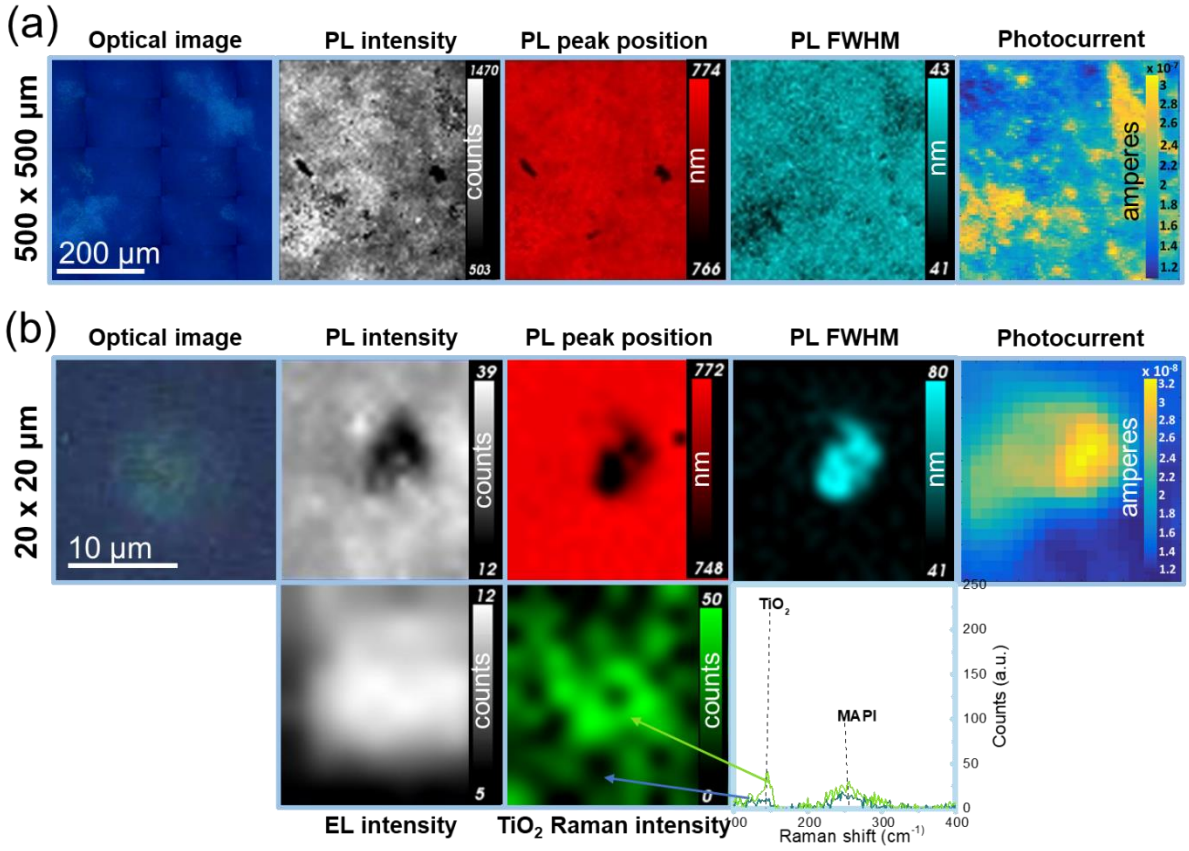

Figure. 4 High-resolution multi-mapping of mesoscopic solar cells fabricated from two-step $MAPbI_3$ solution process. (a) 500 x 500 µm optical microscopic image, PL peak intensity, PL peak position, PL FWHM and photocurrent maps (measured with 1.5 µW laser power). (b) 20 x 20 µm optical image, PL peak intensity, PL peak position, PL FWHM, photocurrent (measured with 0.3 µW laser power), electroluminescence intensity and Raman TiO_2 peak intensity maps measured across a typical feature. Raman single point spectra between 100 cm^{-1} and 400 cm^{-1} measured on and off the feature are also shown.

Cross-sectional scanning electron microscopy

Cross-sectional scanning electron images for the three types of devices are presented in Figure 5a-g. This technique is complimentary to the high-resolution maps as it shows the infiltration of perovskite not only close to the mp-TiO_2 interface but in the entire depth of the mesoporous structure. Low and high magnification cross-sectional images of the one-step $MAPbI_3$ cell are shown in Figure 5a and d, respectively. Elements with higher Z values have lower penetration of the secondary electrons (SE) and an increased signal count. This results in an increased SE signal from the Pb-containing phases and eventually brighter appearing areas, which allows the identification of infiltrated areas with higher perovskite concentrations in the mesoporous stack. The layer stack FTO/mp-TiO_2/mp-ZrO_2/carbon is clearly observed and shows very poor perovskite infiltration for the one-step $MAPbI_3$ device. In fact, perovskite can only be seen in a small portion of the ZrO_2 layer (indicated by the orange circle). These observations do not imply that perovskite was not infiltrated in the mp-TiO_2 layer in some parts of the device, as observed in Figure 2, but there is little chance to cut the sample exactly at these infiltrated areas and observe them on the cross-section. On the contrary, for the one-step AVAI-$MAPbI_3$ cell shown in Figure 5b and e, most of the mp-TiO_2 and mp-ZrO_2 layers are homogeneously infiltrated by the perovskite solution, in good agreement with the multi-mapping results. However, a “trench” is visible where the perovskite

didn't infiltrate the mesoporous layers. The fact that perovskite is also missing in the carbon layer just on top of the trench reveals that a dense carbon flake prevented the perovskite from infiltrating in the layer stack. Energy dispersive spectroscopy (EDS) mapping was realized on a selected area of the cross-section around one larger trench as shown in Figure S9 (some trenches can be up to 10 µm in width, which correlates well with the maps in Figure 3b). As perovskite is identified by its Pb and I elements, it is clear that the perovskite is significantly reduced within the depth of the trench from the carbon to the mp-TiO_2 layer as Pb and I elements are much less present in the trench. The EDS mapping also indicates a higher carbon content just on top of the trench which confirms that a denser carbon flake is present and hinder perovskite infiltration.

The two-step device shown in Figure 5c and f has a more complex morphology. Here, both the mp-TiO_2 and mp-ZrO_2 layers are relatively well infiltrated with perovskite but it can be observed that perovskite doesn't form a continuous film, on the contrary to the one-step AVAI-$MAPbI_3$ cell. Instead, distinct perovskite grains are visible either in the mp-TiO_2 or mp-ZrO_2 layer (as indicated by the blue circles). This peculiar morphology is in excellent agreement with recent work which details the nucleation and growth mechanisms of sequential deposition, explained as follow:[27],[28] after the first infiltration step, PbI_2 forms a partly amorphous PbI_2 film with crystalline clusters having preferential (001) orientation along the substrate surface. Upon dipping into MAI, amorphous PbI_2 is transported to add to the crystalline clusters leaving areas devoid of PbI_2 around the clusters. Besides, due to Ostwald ripening, clusters of small size merge with the large clusters which grow further and convert to $MAPbI_3$, starting from the surface of the clusters. This process results in localised crystals of $MAPbI_3$ with significantly reduced perovskite concentrations in the surrounding mesoporous lattice, which explains the discontinuous appearance of the $MAPbI_3$ film for the two-step device. From Figure 5c, it can also be seen some areas in the mp-TiO_2 which have more continuous $MAPbI_3$ film (indicated by blue arrow), while the ZrO_2 layer on top is depleted in $MAPbI_3$. It is thought that PbI_2 clusters nucleate first at the bottom of the mesoporous structure, in contact with the c-TiO_2 blocking layer, and form PbI_2 platelets orientated along the substrate surface. As amorphous PbI_2 in the mp-ZrO_2 is transported to crystalline clusters in the mp-TiO_2, it leaves an empty space in the ZrO_2 mesoporous layer where $MAPbI_3$ do not form. Finally, the presence of non-reacted PbI_2 at the bottom of the mp-TiO_2 layer cannot be unambiguously confirmed using EDS owing to the contribution from the perovskite to the EDS signal that could be detected using EDS. However, as MAI reacts preferentially at the surface of the PbI_2 clusters, it forms a compact $MAPbI_3$ layer which denies the MAI solution access to the underlying PbI_2 for conversion. This is then more likely that unreacted crystalline PbI_2 can be trapped at the bottom of the mp-TiO_2 layer, as explained by Ummadisingu and Grätzel in other work.[27]

The SEM cross-sectional observations are in excellent agreement with the results obtained with the mapping techniques and show dramatic differences in terms of perovskite infiltration, homogeneity and morphology, which are summarized in Figure 5g-i. It is clear that the one-step $MAPbI_3$ cell suffers from poor perovskite infiltration in the mesoporous structure, where only micrometre-sized areas are infiltrated all the way until the c-TiO_2 interface, which explains the very poor efficiency measured for this cell. On the contrary, the one-step AVAI-$MAPbI_3$ cell displays a highly uniform perovskite film in the mp-TiO_2 layer due to proper infiltration through the entire structure. This is consistent with results from Mei et al. who observed much denser filling of the TiO_2 pores with AVAI- $MAPbI_3$ as compared to $MAPbI_3$.[1] This was explained by a templating action of the AVAI which affects the perovskite crystal nucleation and growth within the mesoporous TiO_2 scaffold. However, it is observed here that dense carbon flakes can prevent perovskite infiltration in some areas, which could affect light collection in these regions. Hence, it is thought that device fabrication process could be optimized to avoid such effect. The perovskite solution could be infiltrated directly in the mp-ZrO_2 and mp-TiO_2 layers without carbon, before depositing a top electrode at low temperature (using graphene for example). The mesoporous carbon layer formulation could also be modified to obtain a more uniform layer and avoid the formation of dense flakes. For the case of the two-step $MAPbI_3$ cell, the morphology of the perovskite layer is more complex. It is clear from the mapping correlations that several types of features are present with either beneficial or detrimental effects on the photocurrent. It

is thought that the mechanisms of sequential deposition should be better controlled to obtain more uniform nucleation of PbI_2 clusters in the mp-TiO_2 and consecutive $MAPbI_3$ growth.

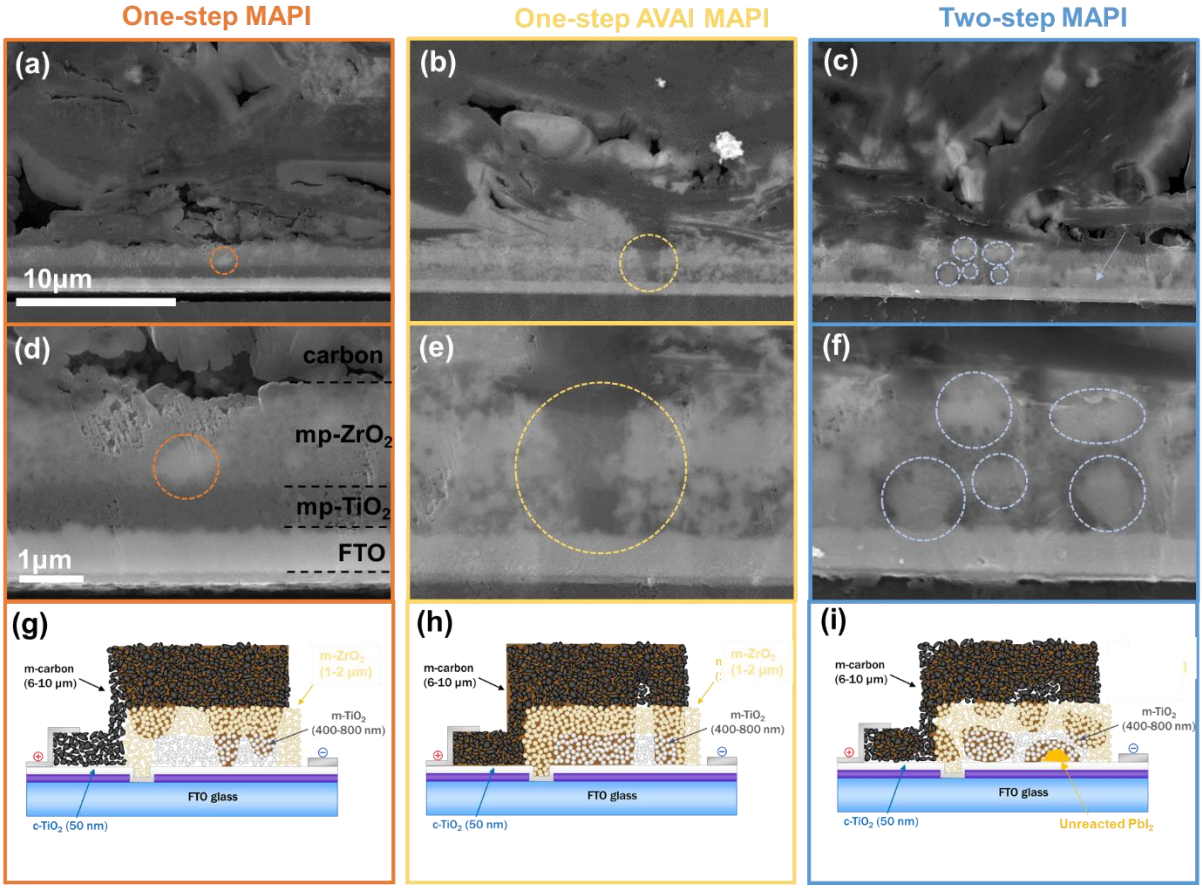

Figure. 5 High and low magnification cross-sectional secondary electron microscopy images of mesoscopic perovskite solar cells based on (a, d) one-step $MAPbI_3$, (b, e) one-step AVAI-$MAPbI_3$ and (c, f) two-step $MAPbI_3$. Cartoon showing mesoscopic perovskite solar cell structure and perovskite infiltration using (g) one-step $MAPbI_3$, (h) one-step AVAI-$MAPbI_3$ or (i) two-step $MAPbI_3$ processes.

CONCLUSIONS

Combining high-resolution photoluminescence, electroluminescence, Raman and photocurrent mapping on the same area with cross-sectional SEM measurements, this study provides unprecedented insights into infiltration mechanisms and electronic transport properties in mesoscopic perovskite solar cells. We have demonstrated that when using one-step deposition process, 5-ammonium valeric acid (AVAI) is key to induce better pore filling in the mesoporous structure. Without AVAI, only around 4% of the cell's area is fully infiltrated and provides efficient electronic coupling with the TiO_2 extraction layer, which explains the poor device short-circuit current in this case. When AVAI is used, around 98% of the cell's area is effective in delivering photocurrent, but dense microscale carbon flakes still prevent perovskite infiltration in some areas and induce current losses. Quite differently, when using a two-step deposition process, a complex perovskite morphology is observed with isolated grains separated by areas of low perovskite concentration, which forms a discontinuous network. This is ascribed to the intercalation of MAI between

crystalline PbI_2 clusters, and then structural reorganisation into $MAPbI_3$. It is thought that small amount of non-reacted PbI_2 is more likely to remain at the interface with the c-TiO_2 blocking layer which could improve photocurrent extraction at this interface. These results motivate further work to achieve better infiltration and homogeneity of the perovskite film in mesoporous devices. Besides, our results provide key insights that could also be applied to characterize devices with planar structure. Although infiltration mechanisms are not an issue for planar devices, variations in electronic contact at interfaces could be monitored using these multi-mapping techniques. This would allow to develop high-quality contacts that can extract photogenerated carriers more efficiently.

METHODS AND EXPERIMENTAL SECTION

Cell preparation and testing

FTO glass substrates (TEC7, XOP) were etched using a Rofin Nd:YVO4 laser (532 nm, speed of 150 $mm.s^{-1}$), cleaned with Hellmanex solution in deionised water, washed with deionised water and rinsed in acetone and isopropanol, before being O_2 plasma treated. A 50 nm-thick compact TiO_2 layer was deposited via spray pyrolysis at 300°C from a solution of 10% titanium di-isopropoxide bis(acetylacetonate) (Sigma) in isopropanol. The mesoporous triple stack was obtained via screen printing of commercial pastes: first, the TiO_2 layer (30 NRD Dyesol, diluted 1:1 by weight with terpineol), followed by sintering at 550°C for 30 minutes; then the ZrO_2 layer (ZT/SP Solaronix), sintered at 400°C for 30 minutes; finally, the carbon layer (Gwent Electronic Materials), sintered at 400°C for 30 minutes, as previously reported.[16],[13]

One-step $MAPbI_3$: an equimolar (0.952 M) solution of PbI_2 (TCI Chemicals) and MAI (Dyesol) in GBL (Sigma) was prepared and stirred at 70°C until completely dissolved.[12] It was then infiltrated by drop casting onto the carbon electrode, left at room temperature for 10 min, then annealed in a fan oven at 50°C for 1 h.

One-step AVAI- $MAPbI_3$: The same 0.952 M solution of PbI_2 and MAI in GBL was prepared and 5-ammonium valeric acid iodide (5-AVAI, Dyesol) was added to it in a 3% molar ratio between 5-AVAI and MAI. As for one-step $MAPbI_3$, the solution was drop casted, and the devices left at room temperature for 10 min before being annealed in a fan oven at 50°C for 1 h.

Two-step $MAPbI_3$: a 1.2 M PbI_2 solution dissolved in N,N-dimethylformamide (DMF) at 70°C was used to infiltrate the mesoporous stack kept at 70°C on a hot plate; after 30 minutes, the cells were cooled down to RT and immersed in a 10 mg/ml MAI solution in IPA for 30 min at room temperature and then annealed for 10 min in a fan oven at 100°C.[18]

Silver paint was applied to the contacts prior to measurements and the 1 cm^2 active area was masked to 0.49 cm^2 using laser-cut black adhesive masks. Current density - voltage (JV) measurements were carried out using a class AAA solar simulator (Newport Oriel Sol3A) under 1 sun illumination conditions, calibrated against a KG5 filtered silicon reference cell (Newport Oriel 91150-KG5), and a Keithley 2400 source meter. The devices were scanned from V_{oc} to J_{sc} and *vice versa* at a scan rate of 130 $mV \cdot s^{-1}$.

High-resolution multi-mapping

Multi-mapping measurements were carried out using a Renishaw InVia confocal Raman microscope in backscattering configuration by measuring the samples through the glass substrates. All measurements were performed under nitrogen atmosphere in an electrical chamber (LTS420E, Linkam Scientific Instrument) mounted directly to a X-Y scanning stage (100 nm minimum step size). Utilising the scanning stage, maps are produced with individual spectra at each region. All measurements were conducted with a 50x objective lens (NA = 0.50). For Photoluminescence, photocurrent and Raman maps, a 532 nm laser excitation source was used (spot size ≈ 1 μm). PL and photocurrent (laser beam-induced current) data were acquired simultaneously at short circuit:

excitation parameters of 1.5 µW laser power (1.5×10^5 mW.cm^{-2}) and 50 ms were used for the large photoluminescence-photocurrent maps (500 x 500 µm), whereas 0.3 µW laser power (3×10^4 mW.cm^{-2}) and 100 ms acquisition time were used for the high-resolution maps (20 x 20 µm). To acquire the photocurrent, the device electrodes were connected to a lock-in amplifier (Stanford Research SR830) with a chopper cutting the laser beam at 134 Hz. Raman spectra were acquired using a laser power of 0.3 mW with an acquisition time of 5 s, whilst individual spectra were acquired in 10 seconds. A source-meter unit (Keithley 236) was used to apply an electrical bias for electroluminescence maps. A bias voltage of 3 V to 5 V and acquisition time of 5 s to 10 s were used to obtain sufficient signal-to-noise ratios. Due to ion migration effect during the EL measurements, 200 seconds were left following the application of the electrical bias before the mapping was started to allow the current to reach equilibrium.

Scanning electron microscopy

Cross sections were prepared after glass cutting using a Hitachi IM4000 Plus Ar broad beam ion miller with a probe current of 4kV for 1.5 hours. Samples were mounted onto a conductive holder and coated in 5nm Pt to provide conductivity for the glass substrate. Imaging was undertaken on a Jeol JSM-7800F Field Emission SEM at 15kV using secondary electron imaging, with EDS detector from Oxford Instruments.

SUPPORTING INFORMATION

Available: carrier generation profile at 532 nm, Schematic carrier dynamic processes in regions of bad and good electronic contact with mp-TiO_2, PL and Raman maps of an empty mp-TiO_2/mp-ZrO_2/mp-carbon stack (before perovskite infiltration), contrasted optical images for the one-step $MAPbI_3$ and one-step AVAI-$MAPbI_3$ C-PSCs, optical microscopy image, PL intensity and photocurrent maps of the two-step $MAPbI_3$ cell taken at 3 different regions, SEM-EDS cross-sectional maps of a one-step AVAI-$MAPbI_3$ mesoscopic perovskite solar cell. This material is available free of charge via the Internet at http://pubs.acs.org.

AUTHOR INFORMATION

Corresponding Author

*E-mails: jeremy.barbe@swansea.ac.uk, w.c.tsoi@swansea.ac.uk.

Author Contributions

The manuscript was written through contributions of all authors. All authors have given approval to the final version of the manuscript.

CONFLICTS OF INTEREST

There are no conflicts to declare.

ACKNOWLEDGEMENTS

We would like to acknowledge Renishaw plc, the M2A funding from the European Social Fund through the Welsh Government, Supergen Solar Challenge (EP/M025020/1), the assistance provided by the Swansea University College of Engineering AIM facility, which was funded in part by the EPSRC (EP/M028267/1), the European Regional Development Fund through the Welsh Government (80708) and the Ser Solar project via Welsh Government.

REFERENCES

(1) Mei, A.; Li, X.; Liu, L.; Ku, Z.; Liu, T.; Rong, Y.; Xu, M.; Hu, M.; Chen, J.; Yang, Y.; Grätzel, M.; Han, H. A Hole-Conductor-Free, Fully Printable Mesoscopic Perovskite Solar Cell with High Stability. *Science.* **2014**, *345* (6194), 295–298.

(2) Chen, H.; Yang, S. Carbon-Based Perovskite Solar Cells without Hole Transport Materials: The Front Runner to the Market ? *Adv. Mater.* **2017**, *29* (24).

(3) Alberola-Borràs, J. A.; Baker, J. A.; De Rossi, F.; Vidal, R.; Beynon, D.; Hooper, K. E. A.; Watson, T. M.; Mora-Seró, I. Perovskite Photovoltaic Modules: Life Cycle Assessment of Pre-Industrial Production Process. *iScience* **2018**, *0* (0), 1–10.

(4) Zhang, H.; Wang, H.; Williams, S. T.; Xiong, D.; Zhang, W.; Chueh, C. C.; Chen, W.; Jen, A. K. Y. $SrCl_2$ Derived Perovskite Facilitating a High Efficiency of 16% in Hole-Conductor-Free Fully Printable Mesoscopic Perovskite Solar Cells. *Adv. Mater.* **2017**, *29* (15).

(5) Liu, S.; Huang, W.; Liao, P.; Pootrakulchote, N.; Li, H.; Lu, J.; Li, J.; Huang, F.; Shai, X.; Zhao, X.; Shen, Y.; Cheng, Y.; Wang, M.. 17% Efficient Printable Mesoscopic PIN Metal Oxide Framework Perovskite Solar Cells Using Cesium-Containing Triple Cation Perovskite. *J. Mater. Chem. A* **2017**, *5* (44), 22952–22958.

(6) NREL Best Research-Cells Efficiency https://www.nrel.gov/pv/.

(7) Yang, W. S.; Park, B.-W.; Jung, E. H.; Jeon, N. J.; Kim, Y. C.; Lee, D. U.; Shin, S. S.; Seo, J.; Kim, E. K.; Noh, J. H.; Seok, S.I. Iodide Management in Formamidinium-Lead-Halide Based Perovskite Layers for Efficient Solar Cells. *Science.* **2017**, *356* (6345), 1376–1379.

(8) Hashmi, S. G.; Martineau, D.; Dar, M. I.; Myllymäki, T. T. T.; Sarikka, T.; Ulla, V.; Zakeeruddin, S. M.; Grätzel, M. High Performance Carbon-Based Printed Perovskite Solar Cells with Humidity Assisted Thermal Treatment. *J. Mater. Chem. A* **2017**, *5* (24), 12060–12067.

(9) Grancini, G.; Roldán-Carmona, C.; Zimmermann, I.; Mosconi, E.; Lee, X.; Martineau, D.; Narbey, S.; Oswald, F.; De Angelis, F.; Graetzel, M.; Nazeeruddin, M.K. One-Year Stable Perovskite Solar Cells by 2D/3D Interface Engineering. *Nat. Commun.* **2017**, *8*, 1–8.

(10) Priyadarshi, A.; Haur, L. J.; Murray, P.; Fu, D.; Kulkarni, S.; Xing, G.; Sum, T. C.; Mathews, N.; Mhaisalkar, S. G. A Large Area (70 cm^2) Monolithic Perovskite Solar Module with a High Efficiency and Stability. *Energy Environ. Sci.* **2016**, *9* (12), 3687–3692.

(11) Bashir, A.; Shukla, S.; Lew, J. H.; Shukla, S.; Bruno, A.; Gupta, D.; Baikie, T.; Patidar, R.; Akhter, Z.; Priyadarshi, A.; Mathews, N.; Mhaisalkar, S.G. Spinel Co_3O_4 Nanomaterials for Efficient and Stable Large Area Carbon-Based Printed Perovskite Solar Cells. *Nanoscale* **2018**, *10* (5), 2341–2350.

(12) Hu, Y.; Si, S.; Mei, A.; Rong, Y.; Liu, H.; Li, X.; Han, H. Stable Large-Area (10×10 cm^2) Printable Mesoscopic Perovskite Module Exceeding 10% Efficiency. *Sol. RRL* **2017**, *1* (2), 1600019.

(13) De Rossi, F.; Baker, J. A.; Beynon, D.; Hooper, K. E. A.; Meroni, S. M. P.; Williams, D.; Wei, Z.; Yasin, A.; Charbonneau, C.; Jewell, E. H.; Watson, T.M. All Printable Perovskite Solar Modules with 198 cm^2 Active Area and Over 6% Efficiency. *Adv. Mater. Technol.* **2018**, *1800156*, 1–9.

(14) Domanski, K.; Correa-Baena, J. P.; Mine, N.; Nazeeruddin, M. K.; Abate, A.; Saliba, M.; Tress, W.; Hagfeldt, A.; Grätzel, M. Not All That Glitters Is Gold: Metal-Migration-Induced Degradation in Perovskite Solar Cells. *ACS Nano* **2016**, *10* (6), 6306–6314.

(15) Niu, G.; Guo, X.; Wang, L. Review of Recent Progress in Chemical Stability of Perovskite Solar Cells. *J. Mater. Chem. A* **2015**, *3* (17), 8970–8980.

(16) Meroni, S. M. P.; Mouhamad, Y.; De Rossi, F.; Pockett, A.; Baker, J.; Escalante, R.; Searle, J.; Carnie, M. J.; Jewell, E.; Oskam, G.; Watson, T.M. Homogeneous and Highly Controlled Deposition of Low Viscosity Inks and Application on Fully Printable Perovskite Solar Cells. *Sci. Technol. Adv. Mater.* **2018**, *19* (1), 1–9.

(17) Chen, J.; Xiong, Y.; Rong, Y.; Mei, A.; Sheng, Y.; Jiang, P.; Hu, Y.; Li, X.; Han, H. Solvent Effect on the Hole-Conductor-Free Fully Printable Perovskite Solar Cells. *Nano Energy* **2016**, *27*, 130–137.

(18) Baker, J.; Hooper, K.; Meroni, S.; Pockett, A.; McGettrick, J.; Wei, Z.; Escalante, R.; Oskam, G.; Carnie, M.; Watson, T. High Throughput Fabrication of Mesoporous Carbon Perovskite Solar Cells. *J. Mater. Chem. A* **2017**, *5* (35), 18643–18650.

(19) Eperon, G. E.; Moerman, D.; Ginger, D. S. Anticorrelation between Local Photoluminescence and Photocurrent Suggests Variability in Contact to Active Layer in Perovskite Solar Cells. *ACS Nano* **2016**, *10* (11), 10258–10266.

(20) El-Hajje, G.; Momblona, C.; Gil-Escrig, L.; Ávila, J.; Guillemot, T.; Guillemoles, J.-F.; Sessolo, M.; Bolink, H. J.; Lombez, L. Quantification of Spatial Inhomogeneity in Perovskite Solar Cells by Hyperspectral Luminescence Imaging. *Energy Environ. Sci.* **2016**, *9* (7), 2286–2294.

(21) Mastroianni, S.; Heinz, F. D.; Im, J.-H.; Veurman, W.; Padilla, M.; Schubert, M. C.; Würfel, U.; Grätzel, M.; Park, N.-G.; Hinsch, A. Analysing the Effect of Crystal Size and Structure in Highly Efficient $CH_3NH_3PbI_3$ Perovskite Solar Cells by Spatially Resolved Photo- and Electroluminescence Imaging. *Nanoscale* **2015**, *7* (46), 19653–19662.

(22) DeQuilettes, D. W.; Zhang, W.; Burlakov, V. M.; Graham, D. J.; Leijtens, T.; Osherov, A.; Bulović, V.; Snaith, H. J.; Ginger, D. S.; Stranks, S. D. Photo-Induced Halide Redistribution in Organic-Inorganic Perovskite Films. *Nat. Commun.* **2016**, *7*.

(23) Barbé, J.; Kumar, V.; Newman, M. J.; Lee, H. K. H.; Jain, S. M.; Chen, H.; Charbonneau, C.; Rodenburg, C.; Tsoi, W. C. Dark Electrical Bias Effects on Moisture-Induced Degradation in Inverted Lead Halide Perovskite Solar Cells Measured by Using Advanced Chemical Probes. *Sustain. Energy Fuels* **2018**, *2, 905-914*.

(24) Hooper, K. E. A.; Lee, H. K. H.; Newman, M. J.; Meroni, S.; Baker, J.; Watson, T. M.; Tsoi, W. C. Probing the Degradation and Homogeneity of Embedded Perovskite Semiconducting Layers in Photovoltaic Devices by Raman Spectroscopy. *Phys. Chem. Chem. Phys.* **2017**, *19*, 5246–5253.

(25) Barbe, J.; Newman, M.; LILLIU, S.; Kumar, V.; Lee, H.; Charbonneau, C.; Rodenburg, C.; Lidzey, D. G.; Tsoi, W. Localized Effect of PbI_2 Excess in Perovskite Solar Cells Probed by High-Resolution Chemical-Optoelectronic Mapping. *J. Mater. Chem. A* **2018**.

(26) Ummadisingu, A.; Grätzel, M. Revealing the Detailed Path of Sequential Deposition for Metal Halide Perovskite Formation. *Sci. Adv.* **2018**, *4* (2), 1–9.

(27) Ummadisingu, A.; Steier, L.; Seo, J. Y.; Matsui, T.; Abate, A.; Tress, W.; Grätzel, M. The Effect of Illumination on the Formation of Metal Halide Perovskite Films. *Nature* **2017**, *545* (7653), 208–212.

Supporting Information

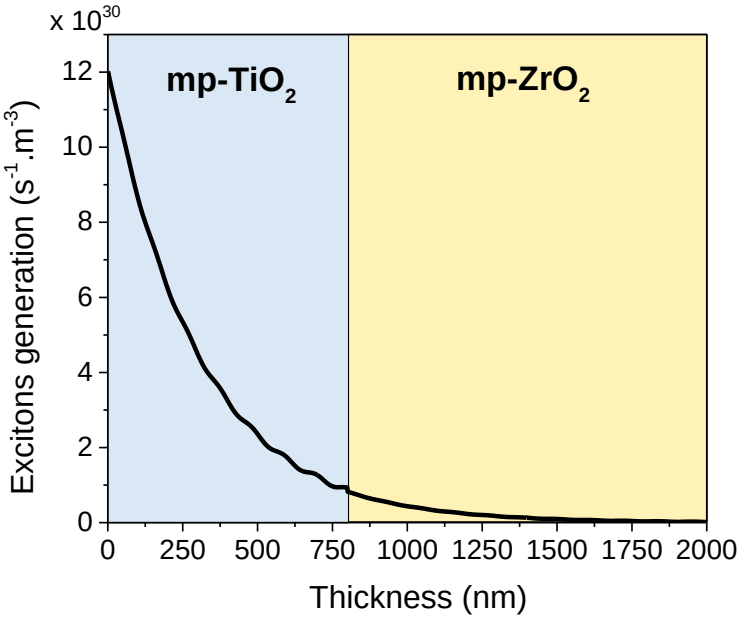

Figure. S1 Carrier generation profile at 532 nm in perovskite infiltrated in mp-TiO_2/mp-ZrO_2 layers (assuming full infiltration and using a laser power of 1.5×10^5 mW.cm^{-2}).

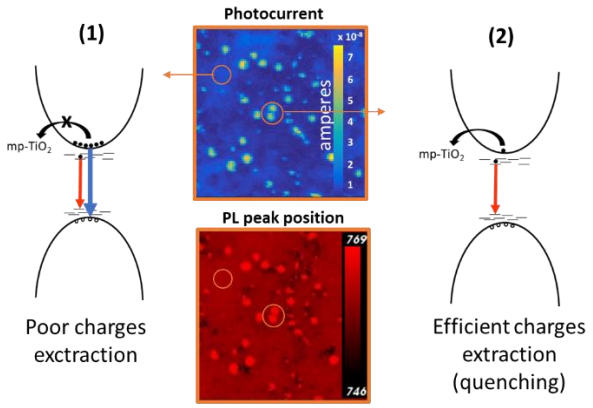

Figure. S2 Schematic carrier dynamic processes in (1) regions of bad electronic contact and (2) regions of good electronic contact with mp-TiO_2 ETL.

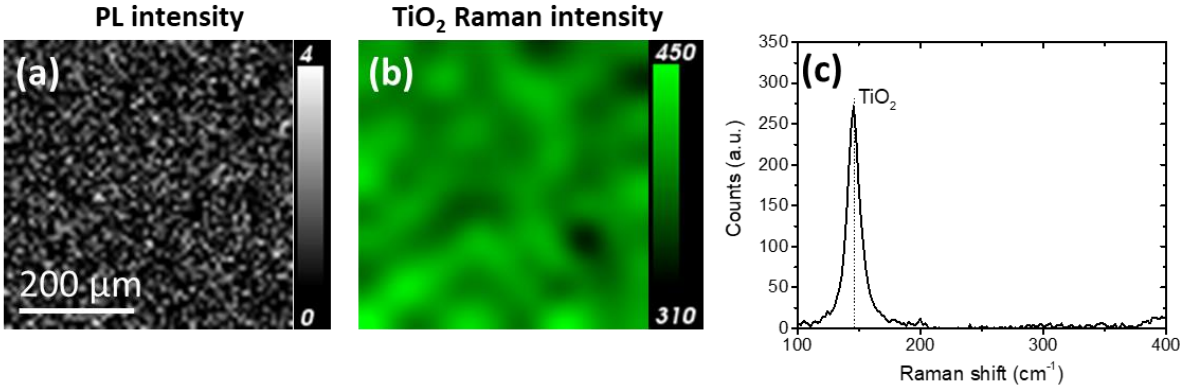

Figure. S3 200 x 200 um maps of an empty mp-TiO_2/mp-ZrO_2/mp-carbon stack (before perovskite infiltration). (a) PL intensity at 775 nm, (b) TiO_2 Raman intensity at 144 cm^{-1}, (c) typical Raman spectrum.

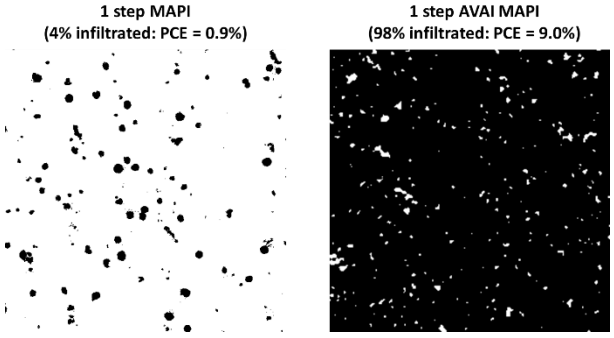

Figure. S4 Binary image of optical images shown in Figure 1a and 2a for the one-step $MAPbI_3$ and one-step AVAI-$MAPbI_3$ C-PSCs, respectively. The infiltrated areas shown in black represent 4% and 98% of the entire surface for the one-step $MAPbI_3$ and AVAI-$MAPbI_3$, respectively.

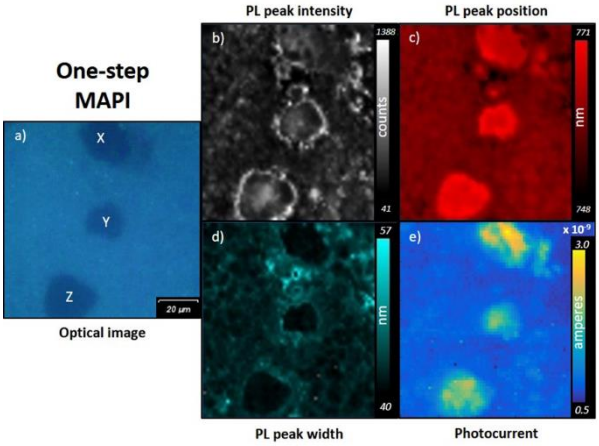

Figure. S5 a) 100 x 100 µm optical micrograph of a one-step MAPI device. b) PL peak intensity map (0.1 s acquisition time, 0.3 µW laser power, 1.5 µm step size). c) PL peak position. d) PL peak width. e) Photocurrent map displaying an increase in photo-generated current over X, Y and Z regions.

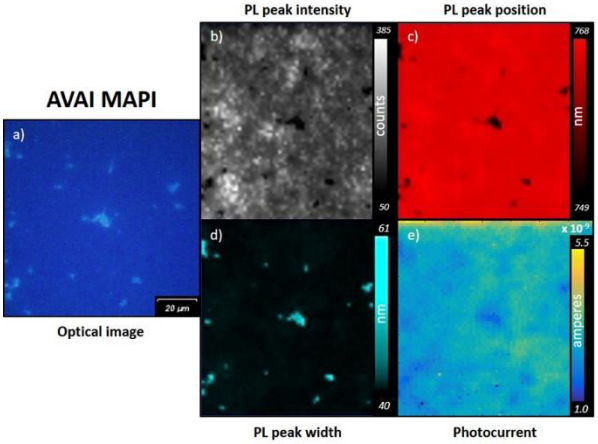

Figure. S6 a) 100 x 100 µm optical micrograph of a cluster of defects on the one-step AVAI MAPI mesoporous carbon perovskite device. b) PL peak intensity map (0.1 s acquisition time, 0.3 µW laser power, 1.5 µm step size). c) PL peak position. d) PL peak width. e) Photocurrent.

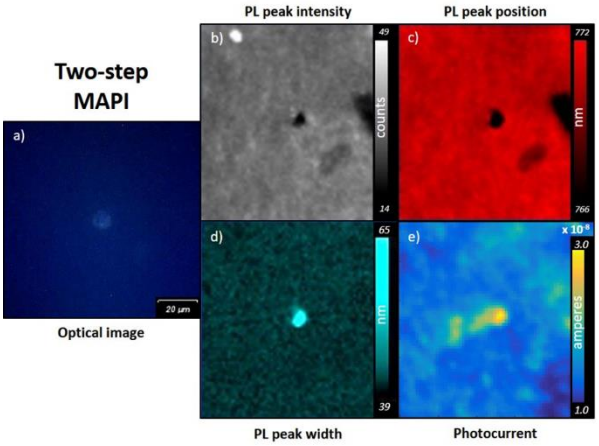

Figure. S7 a) 100 x 100 µm optical micrograph of a defect found on the two-step mesoporous carbon perovskite device. b) PL peak intensity map (0.1 s acquisition time, 0.3 µW laser power, 1.5 µm step size). c) PL peak position. d) PL peak width. e) Photocurrent.

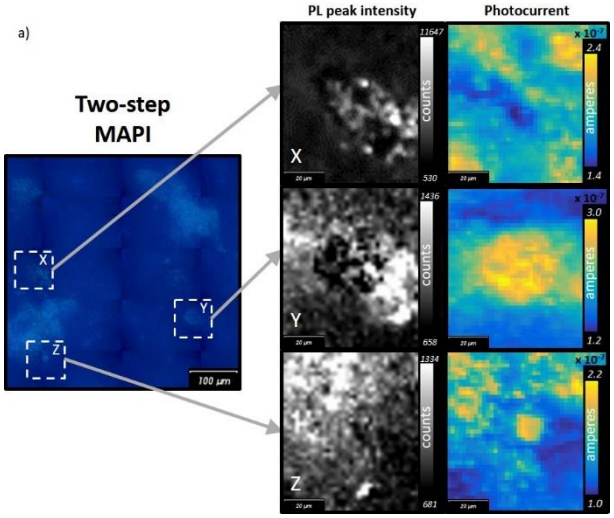

Figure. S8 500 x 500 µm optical microscopy image of the two-step $MAPbI_3$ cell and higher resolution 80x80 µm PL intensity and photocurrent maps taken at 3 different regions showing various PL intensity/photocurrent correlations.

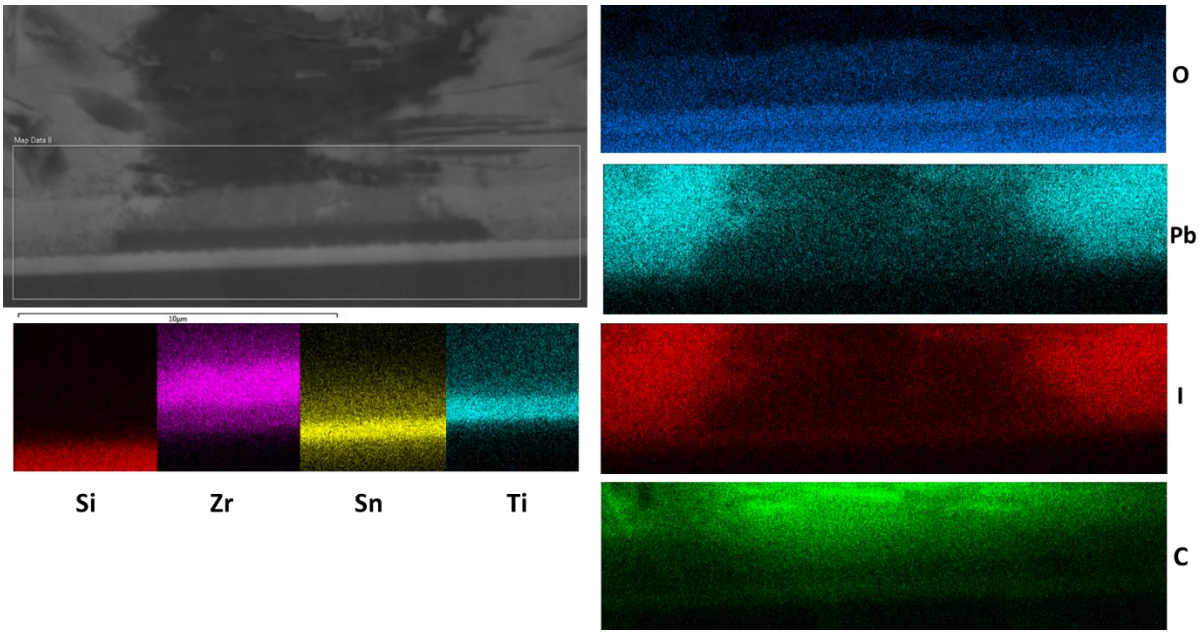

Figure. S9 SEM-EDS cross-sectional maps of a one-step AVAI-$MAPbI_3$ mesoscopic perovskite solar cell. Each layer can be identified by its primary element (C, Zr, Ti, Sn and Si) while the infiltrated $MAPbI_3$ is identified by Pb and I elements. It can be seen that a large carbon flake induces a significant reduction in Pb and I below it, indicating poor perovskite infiltration.